POLARIMETRIC DECOMPOSITION ANALYSIS OF SEA ICE DATA

Mari-Ann N. Moen[1], **Laurent Ferro-Famil** [2,1], **Anthony P. Doulgeris**[1], **Stian N. Anfinsen**[1], **Sebastian Gerland**[3], **and Torbjørn Eltoft**[1,4]

[1]*University of Tromsø, The Auroral Observatory, 9037 Tromsø, Norway, e-mail: Mari-Ann.Moen@uit.no*
[2]*University of Rennes 1, France*
[3]*Norwegian Polar Institute, FRAM centre, 9296 Tromsø, Norway*
[3]*Northern Research Institute, Norway*

ABSTRACT

This paper explores polarimetric properties of Arctic sea ice. The analysis is performed in several steps. First, the SAR image is segmented into distinct classes using an unsupervised classification algorithm, which incorporates both polarimetric and statistical signal features. The algorithm has built in contextual smoothing through Markov Random Field modeling. The image segments are subsequently analyzed by sea ice experts, which based on the SAR data and all available in-situ information gives their opinion about ice type and ice properties. Next, a polarimetric analysis is performed to characterize the segments in terms of polarimetric properties. The analysis clearly shows that areas of thin ice and open water are easily detected. The polarimetry also enables discrimination between smooth surfaces and more deformed ice.

1. INTRODUCTION

The emergence of dual-polarization and fully polarimetric (quad-pol) space-borne SAR systems gives prospects for improvements in the amount of information about sea ice properties that can be obtained from satellite borne sensors. Radar signatures of sea ice are typically complex, and require careful analysis to enable the extraction of useful and accurate surface information. The interpretation of SAR-derived signatures therefore requires a thorough understanding of the interaction of electromagnetic radiation with the snow and ice layers (and ocean), and of how this interaction depends on both surface properties, such as roughness and salinity, and imaging parameters such as frequency, incidence angle, and polarization.

The backscattered signals from sea ice result from a combination of several scattering mechanisms. The relative contributions of rough surface scattering, specular reflections, volume scattering and multiple scattering processes depend on thickness, degree of deformation, size of deformed structures, amount of snow on the ice, salinity and compactness of the ice fragments [1]. Full polarimetric SAR observations allow for the decomposition of radar signals into the contributions from the various scattering mechanisms.

This paper presents the study of a quad polarization SAR scene of Arctic sea ice collected North of Svalbard in April 2011. Ground truth and polarimetric features are used to validate and classify the segments into ice properties. The analysis is performed in several steps. Initially, the SAR image is segmented into distinct classes using an unsupervised classification algorithm, which incorporates both polarimetric and statistical signal features. This algorithm has built in contextual smoothing through Markov Random Field modeling. The resulting classes are thus distinguished from each other by differences in their statistical and polarimetric properties, but they are unlabeled. The image segments are subsequently analyzed by sea ice experts, which based on the SAR data and all available in-situ information gives their opinion about ice type and ice properties. In the second step, a model-based polarimetric decomposition is applied to the PolSAR image to identify the dominant scattering mechanisms. In the final stage, the segmented image is used to mask out image areas associated with the various segments, and each segment is characterized n terms of polarimetric properties.

Sea ice experts also label the segments in the automated segmentation aided by optical photos, thickness data and the Pauli image, which visualizes polarimetric data as an RGB image.

The paper is organized as follows. Section II gives some preliminaries on the physics of sea ice. In section III the segmentation and decomposition algorithms are discussed, and in section IV the results of the analysis is presented. In section gives some conclusions.

2. SEA ICE PRELIMINARIES

The appearance of a SAR image of sea ice is determined by the interaction between the electromagnetic field and the sea ice, and is strongly related to the properties of

the surface and the medium directly below the surface. Sea ice is an inhomogeneous medium composed of an ice background, brine inclusions, air bubbles, and solid salt [2]. Electromagnetic properties of these constituents are characterized by permeabilities and permittivities, which relate material characteristics to electromagnetic fields by constitutive relations [3]. The sea ice constituents are nonmagnetic materials, i.e. their permeability is equal to μ_0, the permeability of vacuum. Except for air, which has permittivity ε_0, the other sea ice constituents have complex permittivities deviating considerably from that of air. This cause reflection and surface scattering at the interface between air and ice , and attenuation and volume scattering within the medium. Ice is a dispersive medium whose complex permittivity changes with electromagnetic wave frequency. The imaginary part of ice permittivity may vary by 2 orders of magnitude as a function of frequency [4]. Both the real and imaginary parts of brine permittivity decrease strongly as frequency increases [5]. The amount of solid salt volume is usually microscopic compared with the other constituents, but the precipitation process of salt at the eutectic temperature redistributes the phase of brine and air inclusions [4]. The effective permittivity of sea ice is determined by how these constituents are mixed with different phases. The permittivity contrasts to the ice background make these inhomogeneities act as scattering sources, when subject to the incident electromagnetic. These inhomogeneities are responsible for effective wave propagation, attenuation, and scattering, which are interrelated and linked to the properties of the constituents in sea ice.

Sea ice can be divided into two major categories, firstyear ice (FY) and multi-year ice (MY). MY-ice has survived at least one summer melt and is discriminated from FY-ice on the basis of properties such as deformation (roughness, surface topography), thickness, salinity and snow cover. Because of winds and currents the Arctic ice pack is kept in almost continuous motion, resulting in significant deformation (i.e. ridging) of the ice. The extent of deformation is exploited when trying to discriminate ice types. The most commonly referred sea ice types are level ice, rafted ice, ridged ice, rubble fields and hummocked ice. Level ice is ice with a relatively flat surface, which has not been deformed to any extent. Rafted ice arises when ice sheets collide and override one another, it occurs usually on new and FY-ice. Pressure processes cause the ice to pile up both above and below the surface. A ridge is the result of such a process and can be described as a long line of piled up, cracked ice. Repeated ridging causes rubble fields. The characteristic hummocky appearance of multiyear ice is due to alternating low refrozen melt ponds and adjacent hummocks. Leads are open water channels in areas of predominantly sea ice. In addition to deformation characteristics there exist several ice types representing young and thin sea ice, which have a large impact on vertical energy fluxes near the surface as well a biota.

The variation in the physical properties of sea ice leads to variations in the radar signals that may allow for type classification. For example, a smooth surface acts as a mirror to microwave illumination and reflects most of the energy away from the radar. Roughness is defined relative to the wavelength, and X-, C- and L-band SAR images (corresponding to the frequencies around 10, 5, and 1 GHz, respectively) will hence image identical surfaces differently due to their sensitivity to different roughness scales. The backscattered signals from sea ice result from a combination of several scattering mechanisms. The relative contributions of rough surface scattering, specular reflections, volume scattering and multiple scattering processes depend on thickness, degree of deformation, size of deformed structures, amount of snow on the ice, salinity and compactness of the ice fragments [1].

3. METHODS

Fig.1 gives a general workflow for the retrieval of information of sea ice from multi-polarization SAR images. The first step is a non-supervised segmentation of the image, which subdivides it into a given number of segments based on variations in statististical and polarimetric properties. This step is followed by a polarimetric analysis, which objective is to describe the polarimetric properties of each image segment. These properties may be interpreted in terms of physical characteristics, which may help labeling the segments as ice types. The final step includes estimating geophysical properties e.g. ice thickness and ice consentration. Here, we mostly address the first two steps.

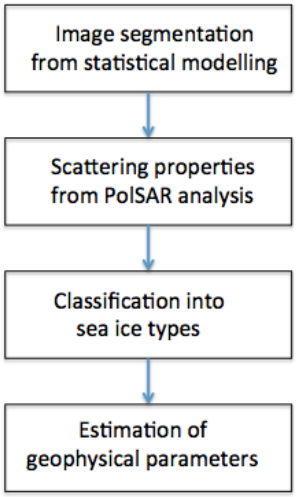

Figure 1. General workflow for sea ice information retreival from PolSAR data.

PolSAR image segmentation
The single-look complex (SLC) PolSAR data, which is generally in the form of as 4×4 Sinclair matrices, is vectorized and multilooked using an $L \times L$ sliding window to create multilook complex (MLC) data in covariance matrix format. Six empirical real-valued features are then

extracted [6]. Given a local neighbourhood of SLC vectors ($\mathbf{s} = [S_{hh}\ , \frac{1}{\sqrt{2}}(S_{hv} + S_{vh})\ , S_{vv}]^T$), the covariance matrix is calculated as:

$$\mathbf{C} = \frac{1}{N}\sum_{i=1}^{L} \mathbf{s}_i \mathbf{s}_i^H \tag{1}$$

where

$$\mathbf{C} = \begin{bmatrix} \left\langle |S_{HH}|^2 \right\rangle & \langle S_{HH} S_{HV}^* \rangle & \langle S_{HH} S_{VV}^* \rangle \\ \langle S_{HV} S_{HH}^* \rangle & \left\langle |S_{HV}|^2 \right\rangle & \langle S_{HV} S_{VV}^* \rangle \\ \langle S_{VV} S_{HH}^* \rangle & \langle S_{VV} S_{HV}^* \rangle & \left\langle |S_{VV}|^2 \right\rangle \end{bmatrix}. \tag{2}$$

The operators $(\cdot)^T$ and $(\cdot)^H$ define the ordinary and the Hermitian transpose operations respectively, and $\langle\cdot\rangle$ is the sample mean over all single-look measurements. The equations defining the features are given in Eqs. (3) - (8), where $d = 3$ is the dimension of the SLC vector.

Relative kurtosis is calculated from SLC and MLC data as described in Eq.(3):

$$RK = \frac{1}{Nd(d+1)} \sum_{i=1}^{N} \left[\mathbf{s}_i^H \mathbf{C}^{-1} \mathbf{s}_i\right]^2. \tag{3}$$

All the other parameters are calculated from MLC data. Their definitions are given below.
Geometric brightness:

$$B = \sqrt[d]{det(\mathbf{C})}. \tag{4}$$

Co-polarization ratio:

$$R_{hh/vv} = \frac{\langle S_{HH} S_{HH}^* \rangle}{\langle S_{VV} S_{VV}^* \rangle}. \tag{5}$$

Cross-polarization ratio:

$$R_{hv/B} = \frac{\langle S_{HV} S_{HV}^* \rangle}{B}. \tag{6}$$

Co-polarization correlation magnitude:

$$|\rho| = \left| \frac{\langle S_{HH} S_{VV}^* \rangle}{\sqrt{\langle S_{HH} S_{HH}^* \rangle \langle S_{VV} S_{VV}^* \rangle}} \right|. \tag{7}$$

Co-polarization correlation angle:

$$\angle\rho = \angle(\langle S_{HH} S_{VV}^* \rangle). \tag{8}$$

The relative kurtosis is a measure of non-Gaussianity. Distributions with high kurtosis tend to have a sharp peak close to the mean, drop quickly and have heavy tails. The relative kurtosis equals one for Gaussian data. The brightness feature represents the total intensity of the multivariate backscatter. Here we have use the geometric mean brightness rather than the span. Both represent the multivariate total intensity. The co-polarization ratio has been shown to be good at separating open water from thin-ice types. Its value is determined by the ice dielectric constant. The largest ratio is observed for open water and new ice, while first-year and multi-year ice have values of ~ 1, [7], [8].
In [8] the HV channel was found to perform very well in discriminating open water and ice. We have defined the cross-polarization ratio as the ratio of cross-pol intensity to geometric brightness. This ratio gives an estimate of the amount of depolarization, and is useful for discriminating ice type and determining ice age. The interpretation of the co-polarization correlation magnitude in sea ice research is yet to be determined [7], but in [9] it is claimed that it is related to both salinity and incidence angle. The co-polarization correlation angle has been shown to be useful for the classification and (proxy) thickness estimation of thin ice types (i.e., $<\sim$ 0.3m) [10], [11]. Its value is determined by the water and ice dielectric constants.

These six features are non-linearly transformed such that the marginal probability density functions (pdfs) have a Gaussian-like appearance. We then model the global pdf as a multivariate Gaussian mixture distribution, and segment the image into a given number of unlabeled segments using the expectation maximition algorithm, as described in [6]. The features were transformed as follows; we use the reciprocal of the relative kurtosis; the next three were logarithmically transformed, the last two were not transformed at all. The number of classes input to the algorithm was manually estimated based on optical images, the Pauli image, the sea ice observation log, and the segmentation results obtained with different number of classes. In addition, the algorithm performs spatial smoothing through Markov random field modelling.

Polarimetric decomposition
In the 3-dimensional Pauli representation, the scattering vector is, under the reciprocity assumption, defined as

$$\mathbf{k}_P = \frac{1}{\sqrt{2}}[s_{hh} + s_{vv}, s_{hh} - s_{vv}, 2s_{hv}], \tag{9}$$

where the square-root factor is used to keep the total backscattered power constant. In the corresponding multilook PolSAR image, each pixel is represented by a 3×3 a coherency matrix T, which is a nonnegative definite, Hermitian matrix. If we additially assume reflection symmetry, the coherence matrix will be of the form

$$\mathbf{T} = \begin{bmatrix} T_{11} & T_{12} & 0 \\ T_{12}^* & T_{22} & 0 \\ 0 & 0 & T_{33} \end{bmatrix} \tag{10}$$

The Freeman decomposition has been successfully applied to analyze the polarimetric data of the forest [12]. The decomposition models the coherency matrix as the contribution of three scattering mechanisms: surface, double-bounce, and volume scattering, i.e.

$$\mathbf{T} = P_s\, \mathbf{T}_s + P_d\, \mathbf{T}_d + P_v\, \mathbf{T}_v, \tag{11}$$

where

$$\mathbf{T}_s = \frac{1}{1+|\beta|^2}\begin{bmatrix} 1 & \beta & 0 \\ \beta^* & |\beta|^* & 0 \\ 0 & 0 & 0 \end{bmatrix}, \qquad (12)$$

$$\mathbf{T}_d = \frac{1}{1+|\alpha|^2}\begin{bmatrix} |\alpha|^* & \alpha & 0 \\ \alpha^* & |\alpha|^* & 0 \\ 0 & 0 & 0 \end{bmatrix}, \qquad (13)$$

$$\mathbf{T}_v = \frac{1}{4}\begin{bmatrix} 2 & 0 & 0 \\ 0 & 1 & 0 \\ 0 & 0 & 1 \end{bmatrix}. \qquad (14)$$

The Freeman-Durden method sometimes produces non-physical solutions for P_s and P_d. To avoid this, we apply a modified form, in which we only remove a fraction of the volume component, i.e., we define $\mathbf{T}_g = \mathbf{T} - a\mathbf{T}_v$, where the multiplying factor a secures that the eigenvalues of $\mathbf{T}_g$ is positive. The decomposition then follows the standard Freeman-Durden decomposition as depicted in Fig.2. We will refer to this decomposition approach as NNED-Freeman-Durden decomposition.

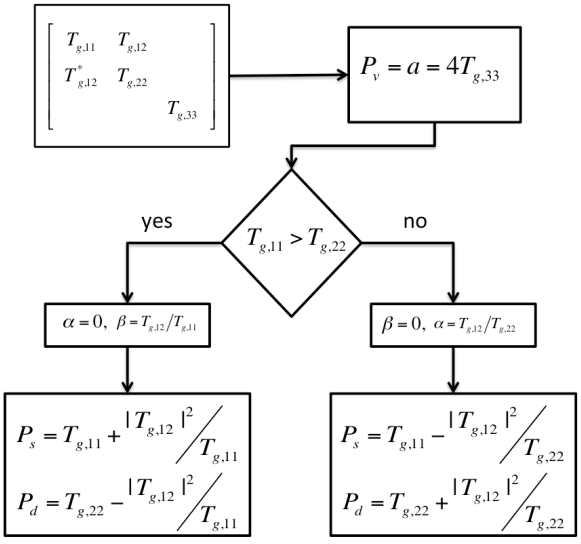

Figure 2. Freeman-Durden decomposition diagram.

4. THE DATASET

Satellite scene: This study only includes the quad-polarization fine mode Radarsat-2 image from 12 April, 2011, which was collected north of Svalbard, as shown in Fig. 3. This image coincides with a good collection of ground truth data. The study area comprised first-year sea ice at different stages of development and leads, both open and refrozen.

Figure 3. Location of Radarsat-2 image, 12 April 2011. Red box north of Svalbard (center 81.1^oN 19.1^oE*).*

Ground truth: Ice thickness measurements over a large area were performed by a helicopter-borne electromagnetic induction sounder (EM-bird)[13]. These flights were also used to collect optical photos and roughness measurements with a laser altimeter. GPS trackers were placed on the ice to track the ice drift between the EM-Bird flight and satellite image acquisition. In addition, an Iridium Surface Velocity Profiler (SVP) buoy was deployed onto the ice on the 11th of April. This buoy transmitted its position hourly, together with other parameters and can was also used for drift calculations. In addition, regular sea ice shipboard observations and photographs from the ship were collected.

5. RESULTS

Fig.4 shows a Pauli image annotated with the original (red track) helicopter track. There is a time span of 1 h 46 min between the satellite image acquisition time and the end EM-bird measurements. The ice drift during this period is significant. Drift measurements from the GPS trackers and the buoy were utilized for to correct for this drift. The drift corrected helicopter track is shown as the white lines in image Fig.4.

The smoothed, geocoded segmentation result is shown in Fig. 5. The image has been segmented into 5 classes. Sea Ice Experts interpreted the segmentation result aided by thickness measurements, optical photos and the Pauli image. Their interpretation is summarized in Table 1.

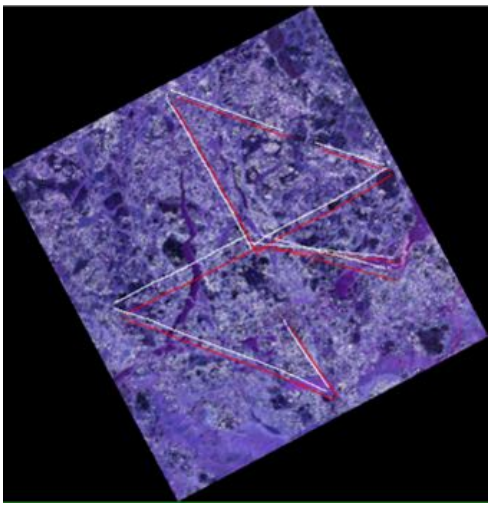

Figure 4. Polarimetriy image shown as Pauli colours. The original helicopter track is shown in red and the ice drift corrected track in white.

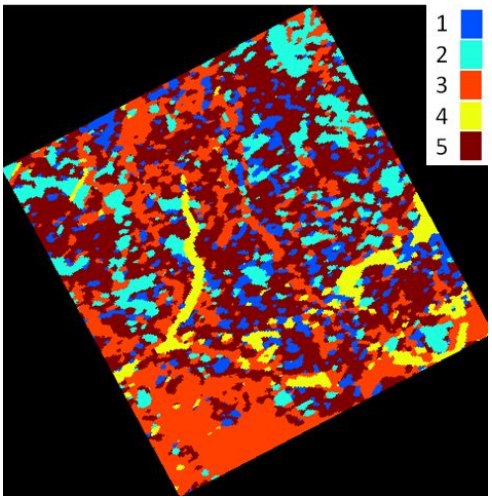

Figure 5. Image segmented by the automated segmentation algorithm, with the number of classes equal to five.

Fig.(6) displays the thickness estimates along the helicopter track. AS can be noted, the thickness varies between 0 and 6-7 meters. Below the thickness curve we have included the image segments along the flight track. By comparing the thickness and the segments, we can conclude that the yellow class certainly corresponds to thin, new frozen ice, or open leads. We also see strong fluctuations in thickness in some classes, indicating the presence of deformed ice.

Figs(7-9) displays the relative contribution of surface scattering, double bounce scattering and volume scattering obtained by the NNED-Freeman-Durden decomposition. It can be seen that the dominant scattering mechanism is surface scattering. Double bounce scattering is almost absent, except for a tiny area in the lower right corner of the image. This area is thought to be characterized by ice broken up by the ship. However, we also

Blue/Brown/ Light Blue	first year ice, different stages of development
Red	Young ice, thin first year ice (sometimes deformed and with snow cover)
Yellow	Thin ice, open water, new ice, nilas, grey ice

Table 1. Class labels produced by sea ice experts

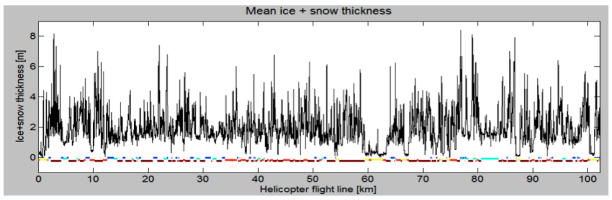

Figure 6. Thickness estimates from EM-bird measurements. The color segments at the bottom corresponds to the segments along the flight track.

see areas of significant volume scattering. Volume scattering is here interpreted as originating from deformed ice. By comparing the decomposition component images, plus some additional polarimetric feature (like *the polarimetric entropy*, *the co-polarization ratio*, and *the coherence between circular RR and LL*), with the segmented classes, we may conclude that brown and the dark blue segments represent more deformed ice with significant volume scattering, where as the other colors are smoother ice, dominated by surface scattering. The yellow class is seen to correspond to very thin ice.

6. SUMMARY AND CONCLUSIONS

This paper presents an analysis of a Radarsat 2 PolSAR scene of Arctic sea ice, collected north of Svalbard in the winter 2011. The scene shows various stages of first year ice, plus some open and refrozen leads. The data set also comprised EM-bird thickness measurements and optical photos along a helicopter track covered by the SAR image. The analysis consisted of a segmentation step, which based on statistical and polarimetric features subdivided the scene into 5 classes. We also applied a non-negative definite Freeman-Durden decomposition on the image to decompose the image into dominant scattering mechanisms. We also tested some other well-known polarimetric parameters, the polarimetric entropy, the co-polarization ratio, and the coherence between LL and RR, in relation to their ability to help labeling the image segments. The analysis show that the segmentation algorithm definitely enable segmentation of sea ice into proper segments, and some of these are easily identified as distinct ice types. The polarimetric information

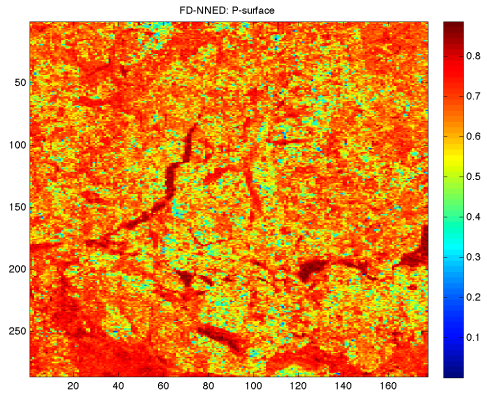

Figure 7. The relative contribution of surface scattering resulting from the NNED Freeman-Durden decomposition.

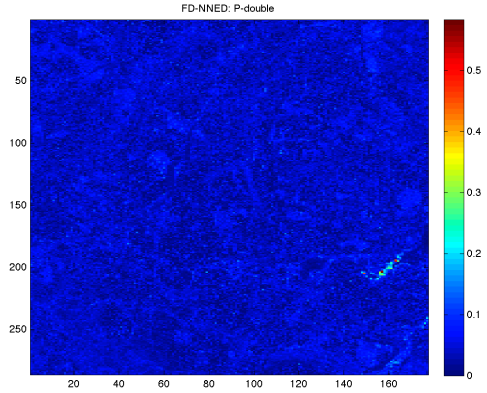

Figure 8. The relative contribution of double bounce scattering resulting from the NNED Freeman-Durden decomposition.

adds information, which allow to distinguish between ice classes of different roughness. Our findings are similar to conclusions made in [14], who claimed they were able classify three ice types by roughness. .

ACKNOWLEDGMENTS

The authors acknowledge the sea experts at the Norwegian Polar Institute for their opinion of the segmented image, Thomas Kræmer at the University of Tromsø for advice in the geocoding, the crew onboard the NoCG Svalbard and the pilots onboard the Governor of Svalbard's OCO Dauphin for their assistance during the research cruise. We also thank the Fram Centre, Tromsø, Norway and RDA Troms for funding.

REFERENCES

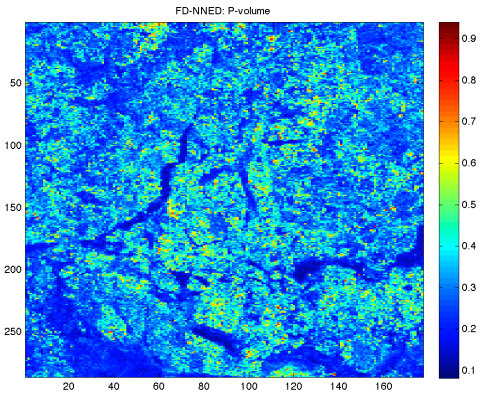

Figure 9. The relative contribution of volume scattering resulting from the NNED Freeman-Durden decomposition.

[1] W. Dierking, A. Carlstrom, and L. M. H. Ulander. The effect of inhomogeneous roughness on radar backscattering from slightly deformed sea ice. *IEEE Trans. Geosci. Remote Sens*, 35(1):147–159, 1997.

[2] S. V. Nghiem, R. Kwok, S. H. Yueh, and M. R. Drinkwater. Polarimetric signatures of sea ice: 1. theoretical model. *J. Geophys. Res.*, 100(C7):13681–13698, 1995.

[3] J. A. Kong. *Electromagnetic Wave Theory*. John Wiley, New York, 1986.

[4] S. Evans. Dielectric properties of ice and snow–a review. *J. Glaciol. Res.*, 5:773–792, 1965.

[5] A. Stogryn and G. J. Desargant. The dielectric properties of brine in sea ice at microwave frequencies. *IEEE Trans. Antennas Propagat.*, 33(5):523–532, 1985.

[6] A.P. Doulgeris and T. Eltoft. Scale mixture of gaussian modelling of polarimetric SAR data. *EURASIP J. Adv. Signal Processing*, pages 1–12, 2010.

[7] R. G. Onsott and R. A. Shuchman. Synthetic aperture radar marine user's manual. In C.R. Jackson and J. R. Apel, editors, *SAR measurements of sea ice*, pages 81–115. NOAA, 2004.

[8] B. Scheuchl, R. Caves, I. Cumming, and G. Staples. Automated sea ice classification using spaceborne polarimetric SAR data. In *Proc. IGARSS 2001*, pages 3117–3119, 2001.

[9] M. R. Drinkwater, R. Kwok, E. Rignot, H. Israelsson, R. G. Onstott, and D. P Winebrenner. Potential applications of polarimetry to the classification of sea ice. In F. D. Carsey, editor, *Microwave remote sensing of sea ice*, number 68 in Geophysical Monograph, pages 419–430. AGU, 1992.

[10] B.B. Thomsen, S.V. Ngheim, and R. Kwok. Polarimetric C-band SAR observations of sea ice in the Greenland Sea. In *Proc. IGARSS 1998*, pages 2502–2504, 1998.

[11] B.B. Thomsen, L.T. Pedersen, H. Skriver, and W. Dierking. Polarimetric EMISAR observations of sea ice in the Greenland Sea. In P. Gudmandsen, editor, *Future Trends in Remote Sensing*, pages 345–351. Taylor & Francis, 1998.

[12] Anthony Freeman and Stephen L. Durden. A three-component scattering model for polarimetric SAR data. *IEEE Trans. Geosci. Remote Sens*, 36(3):963–973, May 1998.

[13] C. Haas, J. Lobach, S. Hendricks, L. Rabenstein, and A. Pfaffling. Helicopterborne measurements of sea ice thickness, using a small and lightweight, digital em system. *J. Appl. Geophys.*, 67(3):234–241, 2009.

[14] J.P.S.Gill and J.J. Yackel. Evaluation of C-band SAR polarimetric parameters for discriminating of first-year sea ice types. *Can. J. Remote Sens.*, 38(3):306–323, 2012.